

*MESHFREE FORMULATION FOR MODELLING OF ORTHOGONAL CUTTING OF
COMPOSITES*

^(a)F. Kahwash¹, ^(a)I. Shyha and ^(b)A. Maheri

^(a)Faculty of Engineering, Northumbria University, Newcastle, UK, NE1 8ST

^(b)School of Engineering, University of Aberdeen, Aberdeen, UK, AB24 3UE

ABSTRACT

The Element-Free Galerkin method (EFG) is a prominent member of the meshfree methods family. In this work, EFG is utilised to simulate the orthogonal cutting process of unidirectional composites. The mathematical model is derived from the weak form of the momentum conservation equation with frictional contact constraints based on penalty method. Spatial discretisation using moving least squares shape functions are used. The onset and progression of damage are predicted by two stress-based failure criteria. Full Newton Raphson solver is used to solve the non-linear system equations iteratively. Numerical experiments investigating the effect of rake angle and fibre orientation are conducted. Cutting forces are compared against experiments and finite element simulations available in literature. Simulations show that the meshfree model is capable of predicting cutting forces as a function of the fibre orientation. Sensitivity analysis is conducted to investigate the effect of important meshfree parameters such as the domain of influence and weight function on forces. One of the strongest advantages of the proposed model is the simple and automatic set up process, as meshing for domain discretisation is not required.

Keywords:

Meshfree; Element-free Galerkin; Orthogonal cutting; Modelling of machining; Unidirectional composites.

¹ Corresponding author's email address: fadi.kahwash@northumbria.ac.uk

1. INTRODUCTION

Global demand for glass fibre reinforced plastic (GFRP) and carbon fibre reinforced plastic (CFRP) is steadily growing [1, 2], with total projected market worth of B\$105.26 by 2021 [3]. Composites are considered as difficult-to-machine materials [4]. This is mainly due to their strong anisotropy, abrasive nature of reinforcement, different behaviour of constituent materials under machining conditions and the complex failure mechanisms [4]. Modelling of machining is utilised to gain fundamental understanding of the machining process and to reduce costly trial and error at the floor shop. Modelling of machining can be analytical, numerical or empirical. The current practice of modelling of composites machining was reviewed in [5]. Extensive research was conducted on numerical modelling of machining composites. The bulk of the research utilised the finite element method (FEM). Interested readers can refer to [4, 6] to review the state of the art in numerical modelling of machining composites.

Orthogonal cutting process is widely used in modelling of machining since it is 2D process and is capable of revealing the basic mechanisms in material removal [7]. The orthogonal cutting process is usually simulated either as a steady state process or as transient process. In the former, the dynamic effects are not considered and the process is assumed quasi-static. This enables the use of implicit solving techniques like Newton Raphson, which is more suitable for cutting at low speeds. The second approach accounts for the dynamic effects and is more suitable for machining at higher speeds. Dynamic studies usually utilise explicit solving techniques such as the central difference method. Studies that used the steady state approach include [8-13]. Some studies that adopted the transient approach include [14-20].

Material modelling is one of the crucial aspects in modelling of machining composites. Two main approaches have been used, macromechanical modelling, and micromechanical modelling. The former assumes the material to be one equivalent phase and sometimes called Equivalent Homogeneous Material. The micromechanical approach models fibres and matrix separately. Most of the studies utilising macromechanical approach used linear elastic material model [8, 9, 11, 13]. However, Zenia [20, 21] used a combined elasto-plastic model with isotropic hardening and without plastic flow in the principle fibre direction.

Material failure and chip formation are important features of the machining simulation. Material failure is governed by composite failure criteria. Different studies used various failure criteria, such as Tsai-Hill [8, 10, 14], maximum stress [10, 11], Hashin [11, 15, 17]. Some studies [8-10] combined two failure mechanisms, primary failure for the onset of chip formation and a secondary failure for the progressive failure and completion of chip formation. The progressive failure was modelled through stiffness degradation concept [11] or continuum damage mechanics approach [15-17] .

In addition to FEM, meshfree (meshless) methods provide a powerful numerical analysis tool. They have been developed to address some of the disadvantages of FEM such as burdensome mesh generation. Currently there are several methods under the umbrella of meshfree methods such as: Smoothed particle hydrodynamics (SPH), Element Free Galerkin (EFG), HP clouds, reproducing kernel particle methods, radial point interpolation method and others. Machining of metals have been studied using some meshfree methods such as: Material Point Method [22], finite pointset method [23] and smoothed particle hydrodynamics [24-28]. Iliescu et al. [29], developed a model for machining composites utilising the discrete element method. The workpiece was modelled as discrete particles with connections. The fibres were modelled as lines of particles closely joint and separated from the neighbouring lines. This allowed investigating the chip formation in comparison with high speed videos at different orientations. The method was able to qualitatively capture the basic failure mechanisms. The accuracy of the cutting force prediction was within $\pm 50\%$ of the experimental values. The Element-Free Galerkin Method (EFG) is a member of the meshfree methods family. The EFG was conceived in Belytschko's seminal paper in 1994 [30]. In the subsequent years, the method undergone many advances and was extended to many engineering applications such as fracture mechanics [31, 32], heat transfer [33, 34], fluid flow calculations [35], metal forming [36], shells [37, 38], plates and laminates [39, 40] and functionally graded materials [41] to name a few. This was due to the suitability of this method in dealing with moving discontinuities, large deformations, and ease of adaptive procedure [42]. However, to the authors' best knowledge, the EFG has not been extended to machining operations, be it metals or composites.

Therefore, this paper aims at simulating the orthogonal cutting process of unidirectional composites using the Element Free Galerkin Method with emphasis on cutting forces as a fundamental output of the model

using the steady state approach. Theoretical formulation of the model will be presented first followed by numerical implementation aspects then the results are presented and discussed.

2. GOVERNING EQUATIONS

In this study, the workpiece is considered as a 2D domain Ω bounded by a boundary Γ governed by:

$$\mathbf{L} \cdot \boldsymbol{\sigma} + \mathbf{b} = \mathbf{0} \quad (1)$$

where, \mathbf{L} is a differential operator, $\boldsymbol{\sigma}$ is the stress tensor, \mathbf{b} the body force. Equation (1) is subject to displacement boundary conditions $\mathbf{u}(\mathbf{x}) = \bar{\mathbf{u}}$; $\mathbf{x} \in \Gamma_u$ and traction boundary conditions $\boldsymbol{\sigma} \cdot \mathbf{n} = \bar{\mathbf{t}}$ $\mathbf{x} \in \Gamma_t$, where, $\bar{\mathbf{u}}$ is the prescribed displacement, \mathbf{n} is the outward normal on Γ_t and $\bar{\mathbf{t}}$ is the prescribed traction along the traction boundary. By applying the variational principle and adding penalty term enforcing the displacement boundary conditions [43], the variation of stationary total potential energy for linear elastic materials can be obtained

$$\delta \Pi \equiv \int_{\Omega} (\mathbf{L} \delta \mathbf{u})^T \mathbf{D} (\mathbf{L} \mathbf{u}) d\Omega - \int_{\Omega} \delta \mathbf{u}^T \mathbf{b} d\Omega - \int_{\Gamma_t} \delta \mathbf{u}^T \bar{\mathbf{t}} d\Gamma - \int_{\Gamma_u} \delta (\mathbf{u} - \bar{\mathbf{u}})^T \alpha_u (\mathbf{u} - \bar{\mathbf{u}}) d\Gamma = 0 \quad (2)$$

where, α_u is a penalty parameter and \mathbf{D} is the material coefficients matrix. Orthogonal cutting problem is a multibody problem where cutting tool and workpiece come into contact. As such contact calculations need to be added to the model.

2.1. FRICTIONAL CONTACT FORMULATION USING PENALTY METHOD

Figure 1 shows a generic case for two discretised bodies in contact. A common way to approach contact calculations is by assuming one body as master and the other as slave. When the slave body moves from configuration Ω_0 to configuration Ω , then the slave node (S) penetrates the master body in the segment M_1M_2 and contact is assumed to have taken place. The local coordinates are defined at the first point of the master segment with outward unit normal (\mathbf{n}) and in plane unit tangent (\mathbf{t}). As a result of the penetration, normal and tangential gap functions are defined as follows:

$$g_n = (\mathbf{u}^S - \mathbf{u}^{M_1}) \cdot \mathbf{n} \quad (3)$$

$$g_t = (\mathbf{u}^S - \mathbf{u}^{M_1}) \cdot \mathbf{t} \quad (4)$$

where, \mathbf{u}^S is the displacement of the slave node, and \mathbf{u}^M is the displacement of the master node,

$$\mathbf{t} = \frac{\mathbf{x}_{M_2} - \mathbf{x}_{M_1}}{\|\mathbf{x}_{M_2} - \mathbf{x}_{M_1}\|} \quad \text{and} \quad \mathbf{n} = \mathbf{t}_3 \times \mathbf{t}, \quad \mathbf{t}_3 \text{ is the out-of-plane unit tangent.}$$

Two basic contact conditions need to be satisfied at the contact boundary, the first is called the *impenetrability condition*, which states that the two bodies cannot occupy the same space at the same time. The second one is the negative traction condition, which states that the traction at the contact boundary should be compressive assuming no welding or adhesion occurs between the bodies. When the normal gap \mathbf{g}_n is negative, the impenetrability condition is violated and contact occurs. The tangential slip expression in Equation (4) represents the sliding movement of the slave node on the boundary of the master body. Using Coulomb friction law, we can distinguish between two cases: the first is when there is no relative motion between the slave node and master body (stick condition). The second is when there is relative sliding between contacting bodies (sliding condition).

In order to satisfy the contact conditions, we construct a penalty functional including both terms of contact [44] [45]

$$P \equiv \int_{\Gamma_c} \alpha_n \frac{g_n^2}{2} d\Gamma + \int_{\Gamma_c} \alpha_t \frac{g_t^2}{2} d\Gamma \quad (5)$$

where, α_n and α_t are penalty parameters. Differentiating with respect to \mathbf{u} gives

$$\delta P \equiv \int_{\Gamma_c} \delta \mathbf{g}_n(\mathbf{u})^T \alpha_n g_n(\mathbf{u}) d\Gamma + \int_{\Gamma_c} \delta \mathbf{g}_t(\mathbf{u})^T \alpha_t g_t(\mathbf{u}) d\Gamma = 0 \quad (6)$$

Using penalty method in imposing constraints has several advantages. The number of unknowns does not increase. The system equations maintain the positive definite property. However, the accuracy of the constraint imposition relies on the choice of a suitable penalty parameter. Theoretically, higher penalty number improves the accuracy, however, in practice, choosing very large penalty parameter could cause ill-conditioning of the system equations.

The constrained variational form of the momentum equation is obtained by adding Equation (6) to Equation (2)

$$\delta\mathbf{\Pi}^* = \delta\mathbf{\Pi} - \delta\mathcal{P} \quad (7)$$

$$\begin{aligned} \delta\mathbf{\Pi}^* \equiv & \int_{\Omega} (\mathbf{L}\delta\mathbf{u})^T \mathbf{D}(\mathbf{L}\mathbf{u}) d\Omega - \int_{\Omega} \delta\mathbf{u}^T \mathbf{b} d\Omega - \int_{\Gamma_f} \delta\mathbf{u}^T \bar{\mathbf{t}} d\Gamma - \int_{\Gamma_u} \delta(\mathbf{u} - \bar{\mathbf{u}})^T \alpha_u (\mathbf{u} - \bar{\mathbf{u}}) d\Gamma \\ & - \int_{\Gamma_c} \delta\mathbf{g}_n(\mathbf{u})^T \alpha_n g_n(\mathbf{u}) d\Gamma - \int_{\Gamma_c} \delta\mathbf{g}_t(\mathbf{u})^T \alpha_t g_t(\mathbf{u}) d\Gamma \end{aligned} \quad (8)$$

Equation (8) can now be discretised using EFG method.

2.2. MOVING LEAST SQUARES APPROXIMATION

In the EFG method, construction of the shape functions is done using moving least squares approximation (MLS) [30]. The approximation of function $u(x)$ field can be expressed as:

$$u^h(x) = \sum_j^m p_j(x) a_j(x) \equiv \mathbf{p}^T(\mathbf{x}) \mathbf{a}(\mathbf{x}) \quad (9)$$

where, $p_j(x)$ is monomial in the space coordinates so that the basis is complete. In this study a 2D linear basis is used $\mathbf{p}^T(\mathbf{x}) = [1, x, y]$. The unknown coefficients a_j can be calculated as follows:

$$\mathbf{a}(\mathbf{x}) = \mathbf{A}^{-1}(\mathbf{x}) \mathbf{B}(\mathbf{x}) \mathbf{u} \quad (10)$$

where, $\mathbf{A}(\mathbf{x}) = \sum_I^n \mathbf{w}_I(\mathbf{x}) \mathbf{p}^T(\mathbf{x}_I) \mathbf{p}(\mathbf{x}_I) \mathbf{u}$; $w_I(x) \equiv w(x - x_I)$ and

$$\mathbf{B}(x) = [w(x - x_1) \mathbf{p}(x_1), w(x - x_2) \mathbf{p}(x_2), \dots, w(x - x_n) \mathbf{p}(x_n)]$$

w is a weight function that depends on the distance between the point of interest and the discrete neighbouring nodes used in calculation, x_I . Finally, the approximated field is expressed as

$$u^h(x) = \sum_{I=1}^n \Phi_I(x) u_I \equiv \mathbf{\Phi}(\mathbf{x}) \mathbf{u} \quad (11)$$

where, Φ_I is the MLS shape function at point of interest I .

$$\Phi_I(x) = \sum_{j=0}^m p_j(x)(A^{-1}(x)B(x))_{jI} \equiv \mathbf{p}^T \mathbf{A}^{-1} \mathbf{B}_I \quad (12)$$

The derivatives of the shape function are required to calculate the strain tensor and they are given below:

$$\Phi_{I,i}(x) = \sum_{j=0}^m \left\{ p_{j,i}(A^{-1}B)_{j,I} + p_j(A_i^{-1}B) + (A^{-1}B_{,j})_{jI} \right\} \quad (13)$$

The used weight functions are the cubic spline and quartic spline respectively:

$$\hat{W}(r_i) = \begin{cases} \frac{2}{3} - 4r_i^2 + 4r_i^3 & r_i \leq 0.5 \\ \frac{4}{3} - 4r_i + 4r_i^2 - \frac{4}{3}r_i^3 & 0.5 < r_i \leq 1 \\ 0 & r_i > 1 \end{cases} \quad (14)$$

$$\hat{W}(r_i) = \begin{cases} 1 - 6r_i^2 + 8r_i^3 - 3r_i^4 & 0 < r_i \leq 1 \\ 0 & r_i > 1 \end{cases} \quad (15)$$

2.3. SPATIAL DISCRETISATION OF THE WEAK FORM

Using the MLS shape functions and their derivatives, Equations (12), (13), the momentum Equation (8) can be discretised. After mathematical treatment the following set of system equations is obtained:

$$(\mathbf{K} - \mathbf{K}^u - \mathbf{K}^C)\mathbf{U} = \mathbf{F} + \mathbf{F}^u + \mathbf{F}^C \quad (16)$$

where, $\mathbf{K}_{IJ} = \int_{\Omega} \mathbf{B}_I^T \mathbf{D} \mathbf{B}_J d\Omega$; $\mathbf{F}_I = \int_{\Omega} \Phi_I^T \mathbf{b} d\Omega + \int_{\Gamma_f} \Phi_I^T \bar{\mathbf{t}} d\Gamma$; $\mathbf{K}^u_{IJ} = \int_{\Gamma_u} \Phi_I^T \alpha_u \Phi_J d\Gamma$;

$\mathbf{F}^u_I = \int_{\Gamma_u} \Phi_I^T \alpha_u \bar{\mathbf{u}} d\Gamma$ and $\mathbf{B}_I = \mathbf{L}\Phi_I$

Using collocation integration, the contact components are given for stick condition

$$\mathbf{K}_{IJ}^C = \alpha_n (\mathbf{n}_I \cdot \mathbf{n}_J^T) + \alpha_t (\mathbf{t}_I \cdot \mathbf{t}_J^T) \quad (17)$$

$$\mathbf{F}_I^C = -(\alpha_n g_n \cdot \mathbf{n}_I + \alpha_t \cdot \mathbf{t}_I) \quad (18)$$

And for slip condition

$$\mathbf{K}_{IJ}^C = \alpha_n (\mathbf{n}_I \cdot \mathbf{n}_J^T) + \mu \alpha_n \text{sign}(g_I) (\mathbf{t}_I \cdot \mathbf{n}_J^T) \quad (19)$$

$$\mathbf{F}_I^C = -\alpha_n g_n \cdot \mathbf{n}_I (1 + \mu \text{sign}(g_I)) \quad (20)$$

where, μ is the friction coefficient

2.4. MATERIAL FAILURE

In order to simulate the onset and progression of damage corresponding to the initiation and completion of chip formation, dual failure scheme is used, partially adopted from Bhatangar et al. [9]. The same study is used for experimental comparison and for material input data. When the tool engages with the workpiece, a primary failure criterion is checked every iteration. The material ahead of the cutting tool is deemed failed if:

$$F_p \equiv \sqrt{\left(\frac{\sigma_n}{F_n}\right)^2 + \left(\frac{\tau}{F_s}\right)^2} \geq 1 \quad (21)$$

where σ_n is the stress normal to the cutting plane in global coordinates, τ is the in-plane shear stress,

F_n is the interface strength in the normal direction and F_s is the shear interface strength. The values of

F_n and F_s are dependent on fibre orientation and are given in Table 1. It was shown by Arola et al.

[46], based on experimental evidence, that chip formation for orientations $0^\circ \leq \theta \leq 90^\circ$ consisted of a dual fracture process, i.e. primary fracture along the cutting plane, mostly due fibre failure and secondary

fracture, mostly due matrix failure, extended along fibre direction to the free surface. In addition,

Bhatangar et al. [9] elaborate that the onset of chip formation is a function of fibre orientation. For

example, at $\theta = 0^\circ$, the failure onset is dominated by matrix cracking while at $\theta = 90^\circ$ it is dominated

by fibre compression. Once two consecutive nodes ahead of the cutting tool have failed, the chip

formation begins and then the secondary (progressive) damage criteria can be triggered. In this study,

maximum stress is adopted. Using this criterion, it is possible to distinguish between tension and

compression modes of failure as well as shear

$$-X^C \leq \sigma_{11} \leq X^T; \quad -Y^C \leq \sigma_{22} \leq Y^T; \quad |\tau_{12}| \leq S_{12} \quad (22)$$

where the stress components are given in the material coordinates, X^T is the tension failure in fibre direction, X^c is the compression failure in failure direction, Y^T is the tension failure in the transverse direction, Y^c failure in compression in the transverse direction and S_{12} the in-plane shear failure. The chip is considered complete when the longitudinal or shear failure reaches the free surface of the workpiece.

2.4.1. STIFFNESS DEGRADATION

Due to the high directionality in stiffness of the unidirectional composite, some modes of failure do not mean complete loss of load bearing in the composite, such as failure in transverse direction. The concept of degrading the stiffness of the composite in certain directions has been used in study composites failure including machining of composites [11, 15, 17]. In this study, the stiffness degradation values were adopted from [47] and are shown in Table 2.

It is generally agreed that fibre failure means a total loss of load carrying capacity, which is why all variables are degraded when longitudinal failure happens. Degradation values of 0.05 were used in [11], we have conducted simulations using 0.01 and 0.05 and found that the effect on force was less significant.

3. IMPLEMENTATION

3.1. SOLVING SCHEME

Full Newton Raphson solver is employed to solve the discretised system equations with displacement increment and bisection option in case of divergence [44]. The code is implemented in MATLAB[®]. The general computational procedure is shown in Figure 3. T is the total simulation time, F_p is the primary failure criteria, which is calculated as per Eqn (21), F_{sec} is the secondary failure criteria as calculated in Eqns (22), δ is the stiffness degradation parameters shown in Table 2 and R is the residual (imbalance between internal and external forces).

3.2. MODEL SET UP

The model set up is shown in Figure 2. The material is assumed to be in plane stress condition. Mechanical properties for the GFRP workpiece are given in Table 3. The geometrical settings of the

model are shown in Table 4. In this study, the tool is considered rigid body and thermal effects are not considered as the cutting speed is chosen to be very low (0.5m/min) in order to reduce the thermal effects to the extent possible. The friction coefficient is taken as $\mu = 0.5$ after Lasri et al. [11]. The effect of the friction coefficient was found minimal in the proposed mode. This is supported by the work of Nayak et al. [10], where they determined the friction coefficient as a function of fibre orientation using pin on disk experiments, then ran simulations with and without friction and found that only thrust force magnitude was marginally affected by friction.

MESHFREE SET UP & PRE-PROCESSING

Accurate numerical integration of the weak form is critical in obtaining meaningful results. Numerical integration of meshfree methods takes two main approaches: (i) mesh based and (ii) nodes based. In this study, cell structure mesh with 2×2 integration points were used, which was found to be accurate and easy to implement, although in nonlinear analysis it can be computationally intensive [36]. Nodal density was increased near the cutting edge to improve the accuracy of the calculations. A total of 9,288 nodes were used in discretisation.

Constructing the domain of influence (DoI) is very important step in calculating the MLS shape functions. The procedure was adopted from [48] and modified:

1. Construct quadrilateral cells and distribute integration points.
2. Calculate cells area.
3. Find cells surrounding each node.
4. Find nodes around each integration point with radial distance $r_I \leq d_{\max} \bar{a}_q$.

where, $d_{\max} \geq 1$ is the scaling parameter which controls the size of the domain and \bar{a}_q is the mean area of the cells surrounding point I . This method provides a robust approach in calculating the domain of influence at any kind of distribution. Where quadrilateral cells are not suitable, triangular cells could be used in the same manner.

4. RESULTS AND DISCUSSION

4.1. CUTTING FORCES

Figure 4 shows the cutting forces comparison between the proposed model, FEM simulations [17] and experimental evidence for three fibre orientations found in [49]. The general trend of forces between the proposed model and the other sources seems to agree. The minimum force was obtained at $\theta = 15^\circ$, while the maximum was obtained at $\theta = 90^\circ$. The values ranged from 21 to 95 N/mm. For $\theta = 30^\circ \rightarrow 60^\circ$, comparison with the experimental data showed that the difference between EFG model and experiments was within $\pm 15\%$ or (less than 5 N/mm), which is comparable to the FEM results shown. By comparing with FEM model, the EFG model under-estimated the forces at lower angles and overestimated them at higher angles. This could be attributed to the different failure mechanisms that are adopted between this study (maximum stress) and that used in [17] i.e. Hashin. At lower θ , shear failure according to failure criteria in Equation (21) has smaller values (refer to Table 1), which indicates that the onset of damage starts fairly quickly triggering the secondary failure criteria. Due to the selective stiffness degradation, failure propagates along fibre direction. Matrix and interface failure quickly reach the free surface of the workpiece and thereby chip formation is complete. On the other hand, at higher angles, the onset of damage is delayed due to the higher values of debonding failure, which leads to a delay in chip completion process and thereby overestimating the force. It is noted that there is a scarcity in data in literature for simulated thrust force at $\gamma = 0^\circ$.

Figure 5 shows the cutting and thrust forces at $\gamma = 5^\circ$ for the EFG model, experimental values given in [9] and FEM results given in [11]. Regarding the cutting force, (Figure 5a), the minimum value of 16N/mm was observed at $\theta = 15^\circ$ and maximum of 64N/mm was observed at $\theta = 90^\circ$. Generally, the trend of forces (as a function of fibre orientation) is matching between EFG and FEM models with experiments. However, the EFG model results seem to be consistently lower than that of experiments and FEM. This could be attributed to the assumption of sharp tool nose in the proposed EFG model as opposed to 0.05mm nose radius in experiments and FEM model. Nose radius increases the force due to reduction of effective rake angle at the nose tip. Soldani et al. [17] studied the effect of nose radius numerically and found that nose edge radius increased the cutting force (~10N/mm increase between 0.05~0.15mm). Adding nose radius to the EFG model caused convergence difficulties for the Newton Raphson solver, therefore it was excluded from the investigation.

Figure 5(b) shows similar comparison but for thrust forces. It is clear that the models considerably underestimated the force magnitude. Lasri et al. [11] argued that the thrust force relies on the bouncing back effect of the machined surface, which creates an upward force on the clearance face [50]. The nature of the quasi-static model and the termination of the calculation after the completion of the first chip suggest that this kind of models have limited capabilities in capturing the bouncing back effect and subsequently the bulk of the thrust force magnitude. This is further compounded by starting the machining process within the workpiece and not at the free edge, which is used to avoid numerical difficulties [9].

Figure 6(a) shows comparison between the proposed EFG model, experiments in [10] and the meshfree model for $\gamma = 10^\circ$. As before, the overall trend is similar although the meshfree model tended to underestimate the force value. This could be attributed to the exclusion of tool nose in the meshfree model as explained earlier. Minimum of 14N/mm was observed at $\theta = 15^\circ$ and maximum of 66N/mm was observed at $\theta = 90^\circ$ compared with minimum of 20N/mm and maximum of 67N/mm for the experiments. Figure 6(b) shows the thrust force comparison, it can be seen that the EFG model predictions is significantly lower than that of the experiments, the same logic applies as in the case of $\gamma = 5^\circ$. However, by comparison with FEM results, FEM showed better agreement with the trend of the experimental values. This could be attributed to the fact that Soldani et al. [17] have used explicit procedure, which allows for simulation of consecutive chip formation. The convergence problems of the quasi-static solver are not found in the explicit algorithm. In the case of $\gamma = 5^\circ$, by comparing the results with [11], where similar solver was used, EFG and FEM results in agreement. This indicates that this is not a drawback in meshfree methods but rather in the chosen solving scheme. This could be addressed by using explicit solver like the central difference method.

4.2. CONVERGENCE STUDIES

In the following section, the effect of discretisation on the forces is studied by changing the nodal density. Then, the effect of the meshfree parameters on the results is examined. Two important parameters are selected, namely, the size of the domain of influence (d_{\max}) and the weight function used in constructing

the MLS approximation. Full factorial design is employed with d_{\max} having values [1, 1.5, 2] and weight function is either cubic or quartic spline.

4.2.1. MESH SIZE/TYPE EFFECTS

Using uniform mesh with the current set up proved infeasible, because of the need for fine mesh at the cutting zone to accurately capture the contact forces. This necessitated using very fine mesh throughout the domain creating out-of-memory errors in the MATLAB code. Instead, non-uniform nodal density distribution is used with highest density near the tool-workpiece interface as shown in Figure 7.

Figure 8 shows the cutting force results of 5 meshes with increased nodal density for $\gamma = 5^\circ$. The results are in close agreement although do not follow the expected convergence behaviour, i.e. approaching the accurate solution from one side. This could be attributed to the following inaccuracies: Using collocation integration of the contact interface meant that small variations in the effective contact length exist among different meshes. This in turn leads to small variations in contact forces. Another possible source of inaccuracy is the triggering of the primary failure criterion. Changes in mesh size leads to change in the energy needed to trigger the primary failure criteria (The damaged area ahead of the cutting tool that would trigger the primary failure decreases with increased nodal density). This can have significant effect at $\theta = 0^\circ$ and $\theta = 90^\circ$ since the primary failure is triggered early in the case of 0° and late in the case of 90° (refer to Table 1) leading to underestimating the force in the former and overestimating it in the latter as the nodal density increases. As such, the mesh with $N = 9288$ nodes is used throughout the study as it provides the best compromise between accuracy (agreement with experimental evidence) and computational time.

4.2.2. THE EFFECT OF DOI SIZE

Figure 9 shows the effect of d_{\max} on cutting force at different rake angles. Generally, higher d_{\max} values yielded lower forces across the different rake angles. This could be explained by the fact that larger domain tends to defuse/smooth high stress gradients. Since the cutting zone is at high stress, the reduced stresses lead to reduced forces. This is further explained by the partition of unity property of the MLS shape function i.e. more nodes in the domain tend to flatten the shape function. d_{\max} has little effect on the trend of the cutting forces.

The effect of d_{\max} on the thrust force is shown in Figure 10. As with the cutting force, the thrust force decreased with increased d_{\max} . Across the range $d_{\max} = 1 \sim 2$, average thrust force was reduced by 10.8% ($\sim 5.3\text{N/mm}$) for $\gamma = 0^\circ$, by 7.9% ($\sim 2.9\text{N/mm}$) $\gamma = 5^\circ$ and by 17% ($\sim 5.7\text{N/mm}$) for $\gamma = 10^\circ$. The fluctuations in Figure 10-a are likely to be due to numerical noise combined with the small magnitude of force which amplified the noise contribution.

4.2.3. THE EFFECT OF WEIGHT FUNCTION

The weight functions used in this study had a negligible effect on the cutting forces for all rake angles, with marginally higher values for cubic weight function at $\gamma = 10^\circ$ as shown in Figure 11.

The effect of the weight function on thrust force is more pronounced, this might be attributed to the very small values of force. Generally, cubic spline yielded higher values: 11.6% for $\gamma = 0^\circ$, 1.4% for $\gamma = 5^\circ$ and 4.9% for $\gamma = 10^\circ$. Figure 12-a showed similar fluctuations to Figure 10-a and for similar reasons. Since higher values of thrust force are more accurate, cubic spline is a better choice for this class of problems.

5. CONCLUSIONS

In this paper, the application of the Element-Free Galerkin Method (EFG) was extended to modelling machining of composites. Moving least squares approximation was used to construct the shape functions with cubic or quartic spline weight functions. Full Newton Raphson solver with bisection capabilities was utilised to solve the system equations. The composites were modelled as Equivalent-homogeneous material in plane stress and with linear elastic behaviour up to failure. Two stress-based failure criteria were used to simulate the onset and progression of chip formation. The cutting forces were calculated using penalty method and regularised Coulomb friction law. The model was validated against experiments and FEM simulations available in literature.

The model was able to capture the strong dependency of the forces on fibre orientations and also the dependency on rake angle. Among the meshfree parameters, the size of DoI was found more significant than weight function. A good rule of thumb for choosing DoI is to use the minimum value that maintains

the invertibility of the \mathbf{A} matrix, see Equation (10). An added advantage of smaller DoI is the reduction of the computational cost as fewer nodes are used in stress calculations at each integration point.

The model was computationally efficient with simulation runtime in the order of 2 hours using a stand-alone PC (Intel i7-4790@3.6GHz and 16GB RAM). The authors were not able to find data on computational runtime in literature of comparable FEM models. It would be interesting to make a comprehensive comparison of total time cost between the proposed meshfree model and similar FEM model (setting up time and computational runtime).

The present model has demonstrated the viability of the EFG model for simulating composites cutting. The pre-processing phase was simple since the nodal connectivity is not required for domain discretisation. This facilitates easy changes in the model (e.g. changing the depth of cut, rake angle, workpiece dimensions) and allows the analyst to concentrate more on analysing the results rather than building the model.

One drawback in the model was the need for some trials to choose a suitable penalty parameter. This is not inherent to the meshfree methods but to the penalty method. Other constraint methods could be employed to alleviate this issue, such as Lagrange multiplier and augmented Lagrangian. Future research effort can include: incorporating dynamic effects (explicit time integration), coding more accurate failure models and utilising more sophisticated approach to chip formation modelling.

ACKNOWLEDGEMENTS

The authors gratefully acknowledge the financial support of Northumbria University for conducting this research.

REFERENCES

1. Holmes, M., *Global carbon fibre market remains on upward trend*. Reinforced Plastics, 2014. **58**(6): p. 38-45.
2. Holmes, M., *Continued growth for European GRP market*. Reinforced Plastics, 2014. **58**(6): p. 28-30.

3. Markets, M.a., *Composites Market- Global Trends and Forecasts to 2021*. 2016.
4. Dandekar, C.R. and Y.C. Shin, *Modeling of machining of composite materials: A review*. International Journal of Machine Tools and Manufacture, 2012. **57**(0): p. 102-121.
5. Kahwash, F., I. Shyha, and A. Maheri, *Modelling of Cutting Fibrous Composite Materials: Current Practice*, in *3rd CIRP Global Web Conference*. 2014, Elsevier B.V.
6. Ben Soussia, A., A. Mkaddem, and M. El Mansori, *Rigorous treatment of dry cutting of FRP – Interface consumption concept: A review*. International Journal of Mechanical Sciences, 2014. **83**: p. 1-29.
7. Caprino, G. and A. Langella, *4 - Analysing cutting forces in machining processes for polymer-based composites*, in *Machining Technology for Composite Materials*, H. Hocheng, Editor. 2012, Woodhead Publishing. p. 75-115.
8. Arola, D. and M. Ramulu, *Orthogonal cutting of fiber-reinforced composites: A finite element analysis*. International Journal of Mechanical Sciences, 1997. **39**(5): p. 597-613.
9. Bhatnagar, N., et al., *Determination of Machining-Induced Damage Characteristics of Fiber Reinforced Plastic Composite Laminates*. Materials and Manufacturing Processes, 2004. **19**(6): p. 1009-1023.
10. Nayak, D., N. Bhatnagar, and P. Mahajan, *Machining studies of UD-FRP composites part 2: finite element analysis*. Machining science and technology, 2005. **9**(4): p. 503-528.
11. Lasri, L., M. Nouari, and M. El Mansori, *Modelling of chip separation in machining unidirectional FRP composites by stiffness degradation concept*. Composites Science and Technology, 2009. **69**(5): p. 684-692.
12. Mkaddem, A., I. Demirci, and M.E. Mansori, *A micro–macro combined approach using FEM for modelling of machining of FRP composites: Cutting forces analysis*. Composites Science and Technology, 2008. **68**(15–16): p. 3123-3127.
13. Rao, G.V.G., P. Mahajan, and N. Bhatnagar, *Three-dimensional macro-mechanical finite element model for machining of unidirectional-fiber reinforced polymer composites*. Materials Science and Engineering: A, 2008. **498**(1–2): p. 142-149.

14. Mkaddem, A. and M. El Mansori, *Finite element analysis when machining UGF-reinforced PMCs plates: Chip formation, crack propagation and induced-damage*. Materials & Design, 2009. **30**(8): p. 3295-3302.
15. Santiuste, C., X. Soldani, and M.H. Miguélez, *Machining FEM model of long fiber composites for aeronautical components*. Composite structures, 2010. **92**(3): p. 691-698.
16. Santiuste, C., H. Miguélez, and X. Soldani, *Out-of-plane failure mechanisms in LFRP composite cutting*. Composite Structures, 2011. **93**(11): p. 2706-2713.
17. Soldani, X., et al., *Influence of tool geometry and numerical parameters when modeling orthogonal cutting of LFRP composites*. Composites Part A: Applied Science and Manufacturing, 2011. **42**(9): p. 1205-1216.
18. Calzada, K.A., et al., *Modeling and interpretation of fiber orientation-based failure mechanisms in machining of carbon fiber-reinforced polymer composites*. Journal of Manufacturing Processes, 2012. **14**(2): p. 141-149.
19. Usui, S., J. Wadell, and T. Marusich, *Finite Element Modeling of Carbon Fiber Composite Orthogonal Cutting and Drilling*. Procedia CIRP, 2014. **14**(0): p. 211-216.
20. Zenia, S., et al., *Numerical analysis of the interaction between the cutting forces, induced cutting damage, and machining parameters of CFRP composites*. The International Journal of Advanced Manufacturing Technology, 2014. **78**(1): p. 465-480.
21. Zenia, S., et al., *An Elastoplastic Constitutive Damage Model to Simulate the Chip Formation Process and Workpiece Subsurface Defects when Machining CFRP Composites*. Procedia CIRP, 2015. **31**: p. 100-105.
22. Naim, J.A., *Numerical simulation of orthogonal cutting using the material point method*. Engineering Fracture Mechanics, 2015. **149**: p. 262-275.
23. Uhlmann, E., R. Gerstenberger, and J. Kuhnert, *Cutting Simulation with the Meshfree Finite Pointset Method*. Procedia CIRP, 2013. **8**: p. 390-395.
24. Madaj, M. and M. Piška, *On the SPH Orthogonal Cutting Simulation of A2024-T351 Alloy*. Procedia CIRP, 2013. **8**(0): p. 152-157.
25. Heisel, U., et al., *Modelling of orthogonal cutting processes with the method of smoothed particle hydrodynamics*. Production Engineering, 2013: p. 1-7.

26. Zahedi, A., et al. *Application of Smooth-Particle Hydrodynamics in Metal Machining*. in *Journal of Physics: Conference Series*. 2012. IOP Publishing.
27. Villumsen, M.F. and T.G. Fauerholdt, *Simulation of metal cutting using smooth particle hydrodynamics*. LS-DYNA. Anwenderforum, Bamberg, 2008: p. 17-36.
28. Limido, J., et al., *SPH method applied to high speed cutting modelling*. International journal of mechanical sciences, 2007. **49**(7): p. 898-908.
29. Iliescu, D., et al., *A discrete element method for the simulation of CFRP cutting*. Composites Science and Technology, 2010. **70**(1): p. 73-80.
30. Belytschko, T., Y.Y. Lu, and L. Gu, *Element -free Galerkin methods*. International journal for numerical methods in engineering, 1994. **37**(2): p. 229-256.
31. Belytschko, T., et al., *Element-free galerkin methods for static and dynamic fracture*. International Journal of Solids and Structures, 1995. **32**(17-18): p. 2547-2570.
32. Belytschko, T. and M. Tabbara, *DYNAMIC FRACTURE USING ELEMENT-FREE GALERKIN METHODS*. International Journal for Numerical Methods in Engineering, 1996. **39**(6): p. 923-938.
33. Singh, A., I.V. Singh, and R. Prakash, *Meshless analysis of unsteady-state heat transfer in semi-infinite solid with temperature-dependent thermal conductivity*. International Communications in Heat and Mass Transfer, 2006. **33**(2): p. 231-239.
34. Zhang, X., P. Zhang, and L. Zhang, *An improved meshless method with almost interpolation property for isotropic heat conduction problems*. Engineering Analysis with Boundary Elements, 2013. **37**(5): p. 850-859.
35. Du, C., *An element-free Galerkin method for simulation of stationary two-dimensional shallow water flows in rivers*. Computer Methods in Applied Mechanics and Engineering, 2000. **182**(1-2): p. 89-107.
36. Li, G. and T. Belytschko, *Element -free Galerkin method for contact problems in metal forming analysis*. Engineering Computations, 2001. **18**(1/2): p. 62-78.
37. Liu, L., L.P. Chua, and D.N. Ghista, *Element-free Galerkin method for static and dynamic analysis of spatial shell structures*. Journal of Sound and Vibration, 2006. **295**(1-2): p. 388-406.

38. Graça, A., R.P.R. Cardoso, and J.W. Yoon, *Subspace analysis to alleviate the volumetric locking in the 3D solid-shell EFG method*. Journal of Computational and Applied Mathematics, 2013. **246**: p. 185-194.
39. Belinha, J. and L.M.J.S. Dinis, *Analysis of plates and laminates using the element-free Galerkin method*. Computers & Structures, 2006. **84**(22–23): p. 1547-1559.
40. Belinha, J. and L.M.J.S. Dinis, *Nonlinear analysis of plates and laminates using the element free Galerkin method*. Composite Structures, 2007. **78**(3): p. 337-350.
41. Wu, C.-P. and S.-W. Yang, *RMVT-based meshless collocation and element-free Galerkin methods for the approximate 3D analysis of multilayered composite and FGM circular hollow cylinders*. Composites Part B: Engineering, 2011. **42**(6): p. 1683-1700.
42. Belytschko, T., et al., *Meshless methods: an overview and recent developments*. Computer methods in applied mechanics and engineering, 1996. **139**(1): p. 3-47.
43. Zhu, T. and S.N. Atluri, *A modified collocation method and a penalty formulation for enforcing the essential boundary conditions in the element free Galerkin method*. Computational Mechanics, 1998. **21**(3): p. 211-222.
44. Kim, N.-H., *Introduction to nonlinear finite element analysis*. 2014: Springer Science & Business Media.
45. Wriggers, P., T. Vu Van, and E. Stein, *Finite element formulation of large deformation impact-contact problems with friction*. Computers & Structures, 1990. **37**(3): p. 319-331.
46. Arola, D., M. Sultan, and M. Ramulu, *Finite element modeling of edge trimming fiber reinforced plastics*. Journal of manufacturing science and engineering, 2002. **124**(1): p. 32-41.
47. Zhao, L.G., N.A. Warrior, and A.C. Long, *Finite element modelling of damage progression in non-crimp fabric reinforced composites*. Composites Science and Technology, 2006. **66**(1): p. 36-50.
48. Liu, G.-R., *Meshfree methods: moving beyond the finite element method*. 2010: CRC press.
49. Nayak, D., N. Bhatnagar, and P. Mahajan, *Machining studies of uni-directional glass fiber reinforced plastic (UD-GFRP) composites part 1: effect of geometrical and process parameters*. Machining science and technology, 2005. **9**(4): p. 481-501.

50. Zhang, L.C., *Cutting composites: A discussion on mechanics modelling*. Journal of Materials Processing Technology, 2009. **209**(9): p. 4548-4552.

ACCEPTED MANUSCRIPT

LIST OF FIGURES

Figure 1: Basic terminology for contact problem

Figure 2: Numerical set up

Figure 3: Flowchart of numerical solving procedure

Figure 4: cutting force comparison at 0° rake and 0.2 mm depth of cut

Figure 5: Cutting forces comparison at 5° rake (a) cutting force, (b) thrust force

Figure 6: Force comparison at 10° rake (a) cutting force, (b) thrust force

Figure 7: Nodal discretisation of domain (a) $N = 3385$, (b) $N = 9288$ and (c) $N = 21621$ nodes

Figure 8: Discretisation sensitivity

Figure 9: Effect of DoI size on cutting force at $\gamma =$ (a) 0° , (b) 5° , (c) 10°

Figure 10: Effect of DoI size on thrust force at $\gamma =$ (a) 0° , (b) 5° , (c) 10°

Figure 11: Effect of weight function on cutting force at $\gamma =$ (a) 0° , (b) 5° , (c) 10°

Figure 12: Effect of weight function on thrust force at $\gamma =$ (a) 0° , (b) 5° , (c) 10°

LIST OF TABLES

Table 1: Normal and shear strength properties [9]

Table 2: Stiffness degradation parameters

Table 3: Mechanical properties for UD-GFRP [9]

Table 4: Geometrical settings of the model

ACCEPTED MANUSCRIPT

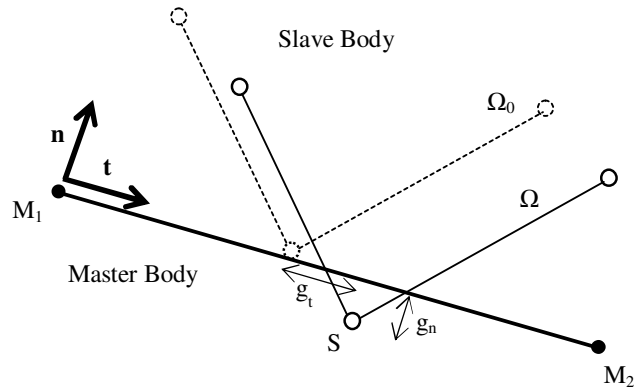


Figure 1: Basic terminology for contact problem

ACCEPTED MANUSCRIPT

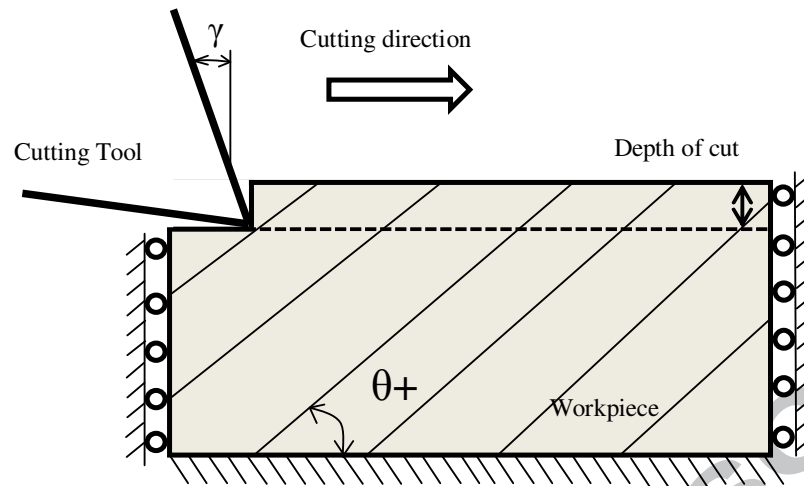


Figure 2: Numerical set up

ACCEPTED MANUSCRIPT

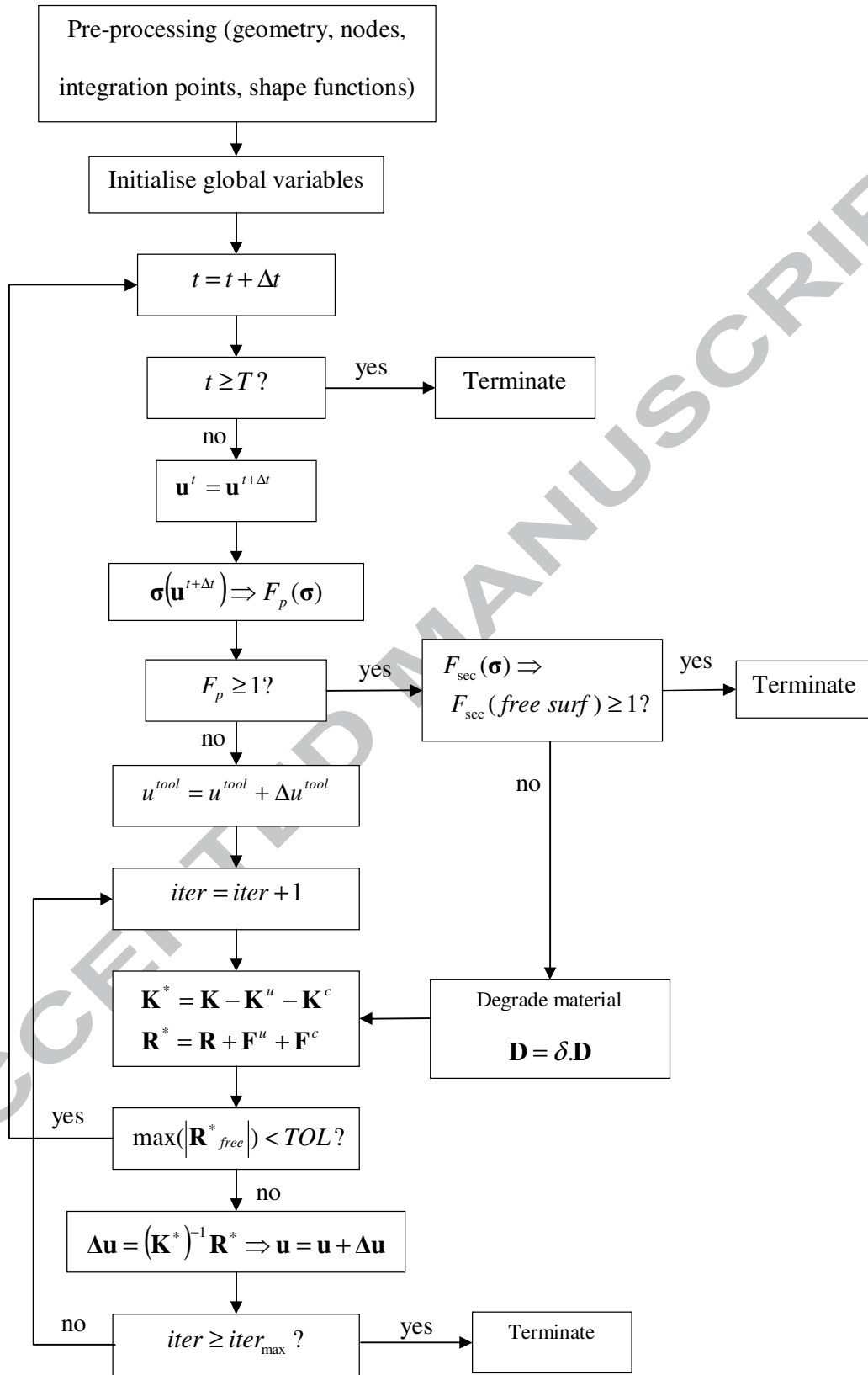


Figure 3: Flowchart of numerical solving procedure

ACCEPTED MANUSCRIPT

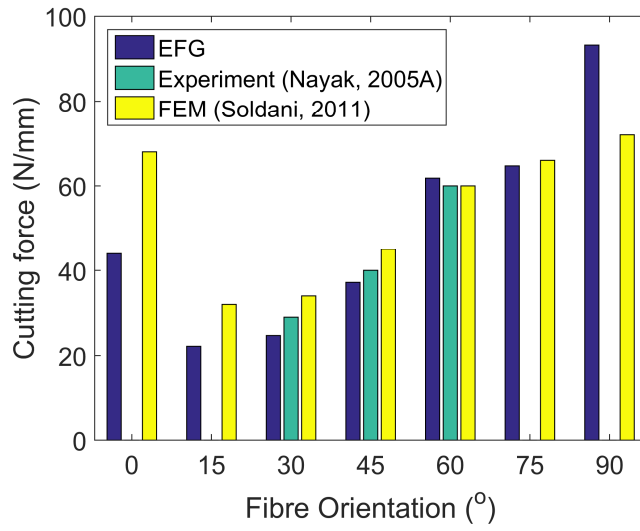


Figure 4: cutting force comparison at 0° rake and 0.2 mm depth of cut

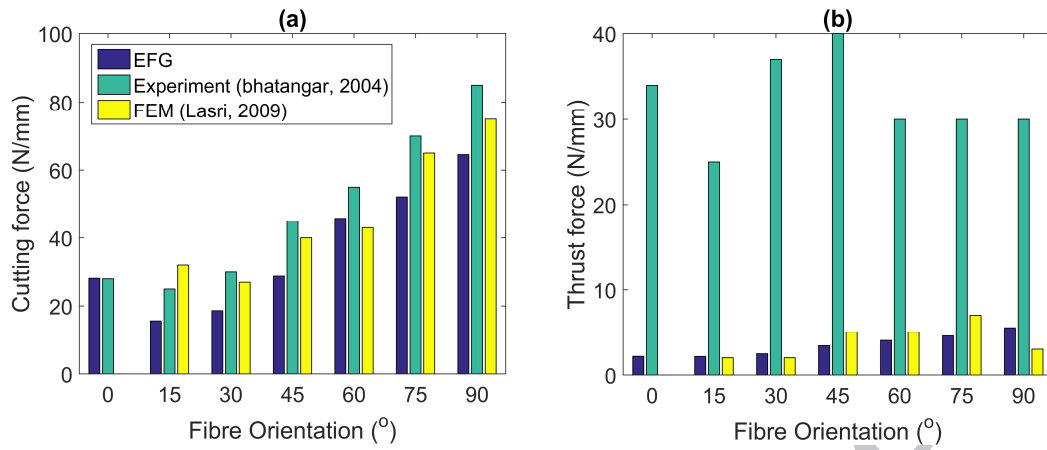


Figure 5: Cutting forces comparison at 5° rake (a) cutting force, (b) thrust force

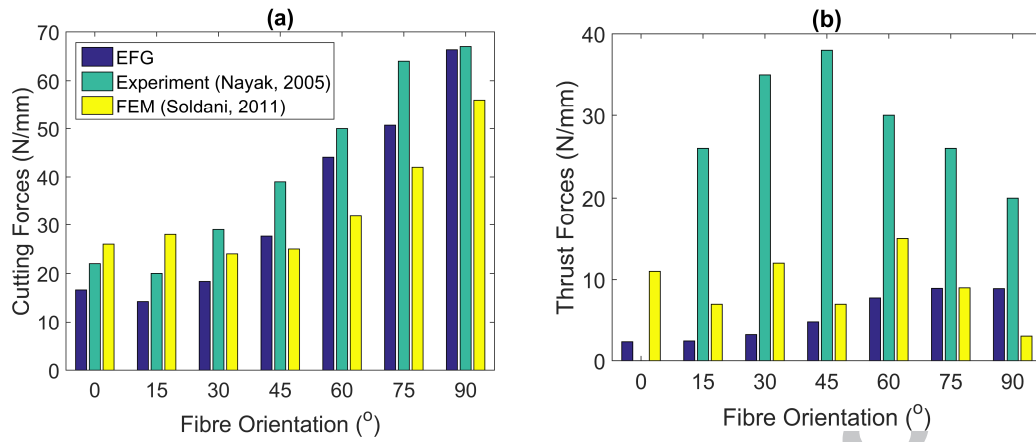


Figure 6: Force comparison at 10° rake (a) cutting force, (b) thrust force

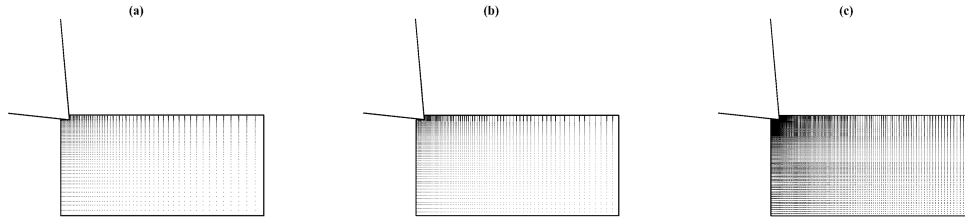


Figure 7: Nodal discretisation of domain (a) $N = 3385$, (b) $N = 9288$ and (c) $N = 21621$ nodes

ACCEPTED MANUSCRIPT

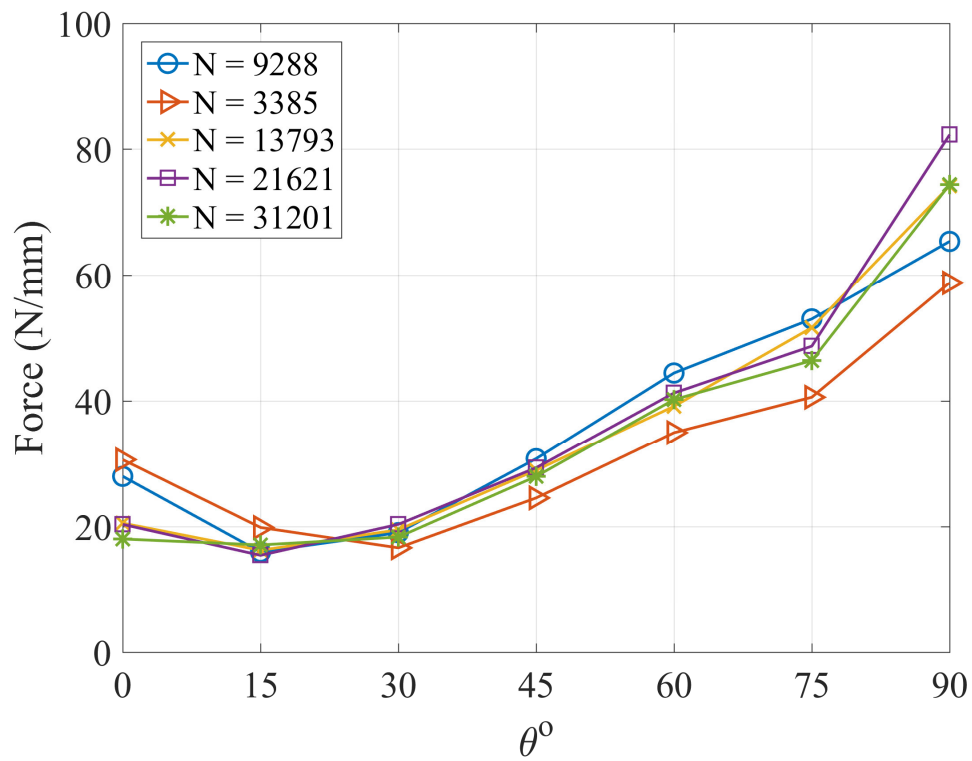


Figure 8: Discretisation sensitivity

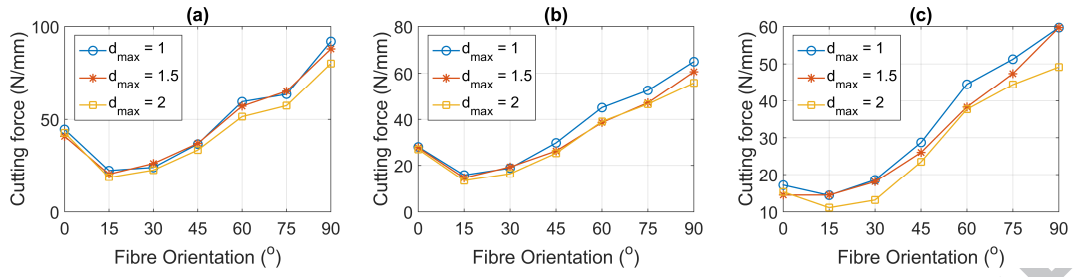


Figure 9: Effect of DoI size on cutting force at $\gamma =$ (a) 0° , (b) 5° , (c) 10°

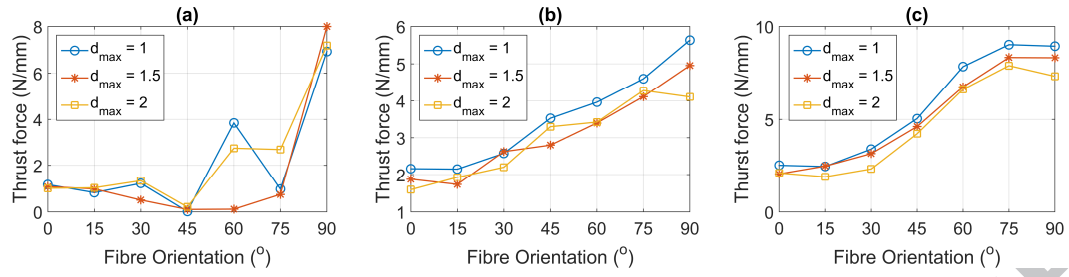


Figure 10: Effect of DoI size on thrust force at $\gamma =$ (a) 0° , (b) 5° , (c) 10°

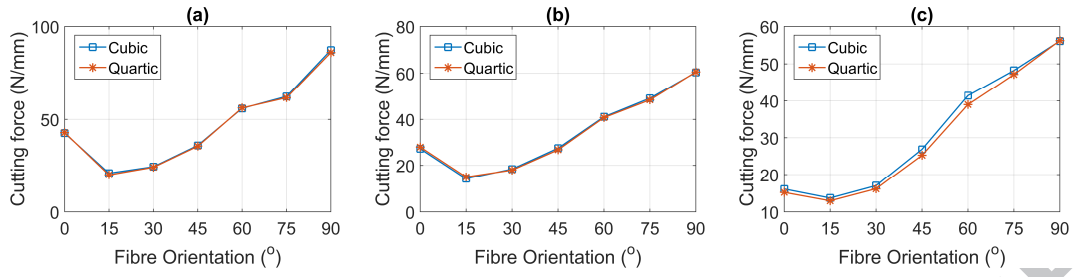


Figure 11: Effect of weight function on cutting force at $\gamma =$ (a) 0° , (b) 5° , (c) 10°

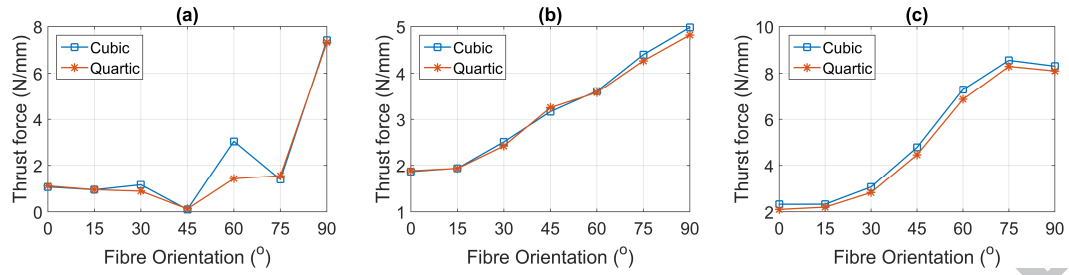


Figure 12: Effect of weight function on thrust force at $\gamma =$ (a) 0° , (b) 5° , (c) 10°

Table 1: Normal and shear strength properties [9]

θ°	0	15	30	45	60	75	90
<i>Normal strength</i> <i>N/mm²</i>	59	87.1302	127.75	379.5	598.25	998.547	1200
<i>Shear strength</i> <i>N/mm²</i>	25	39.822	59.89	96.958	150	180.62	250

ACCEPTED MANUSCRIPT

Table 2: Stiffness degradation parameters

<i>Failure Mode</i>	E_1	E_2	G_{12}
<i>Longitudinal failure</i>	0.01	0.01	0.01
<i>Transverse failure</i>	1	0.01	0.2
<i>In plane shear failure</i>	1	0.01	0.01

ACCEPTED MANUSCRIPT

Table 3: Mechanical properties for UD-GFRP [9]

E_1 (GPa)	E_2 (GPa)	ν_{12}	G_{12} (GPa)	X_T (MPa)	X_C (MPa)	Y_T (MPa)	Y_C (MPa)	S_{12} (MPa)
48	12	0.19	6	1200	800	59	128	25

ACCEPTED MANUSCRIPT

Table 4: Geometrical settings of the model

<i>Workpiece dimensions (mm)</i>	10 × 5
<i>Depth of cut (mm)</i>	0.2
<i>rake angle γ (°)</i>	0, 5, 10
<i>clearance angle (°)</i>	6
<i>Fibre orientation θ (°)</i>	0, 15, 30, 45, 60, 75, 90
<i>Cutting speed (m/min)</i>	0.5

HIGHLIGHTS

- Element-free Galerkin model of orthogonal cutting of composites is developed.
- Discretised equations are derived from the weak form of momentum equation
- Advantages: simple set up and computationally efficient
- Cutting forces results agreed well with experiments and FEM simulations

ACCEPTED MANUSCRIPT